JOURNAL OF PROPULSION AND POWER
Vol. 31, No. 5, September–October 2015

Computational Fluid Dynamics Simulation of Tip-to-Tail for Hypersonic Test Vehicle

Malsur Dharavath,* P. Manna,* and Debasis Chakraborty[†]
Defence Research and Development Laboratory, Hyderabad 500 058, India

DOI: 10.2514/1.B35686

Computational fluid dynamics simulations are carried out for a complete hypersonic vehicle integrating both external (nonreacting) and internal (reacting) flow together to calculate the scramjet combustor performance and vehicle net thrust minus drag. Simulations are carried out for a flight Mach number of about six. Three-dimensional Navier–Stokes equations are solved along with the shear stress transport k-ω turbulence model and single-step chemical reaction based on fast chemistry. The Lagrangian particle tracking method for droplets is used for combustion of kerosene fuel. Flow is largely nonuniform at the inlet of the combustor. Mass flow of ingested air increases with increase in angle of attack. Because of more combustion of fuel, wall surface pressure is higher for $\alpha = 6$ deg compared with $\alpha = 0$ deg. Combustion efficiency and thrust achieved are found to increase with the increase in angle of attack. Considerable amount of thrust is obtained from a single expansion ram nozzle and achievement of positive thrust–drag for the whole vehicle is demonstrated. The computational analysis of the whole vehicle provides net forces and moments of the whole vehicle, which is very useful for the mission analysis of the vehicle.

Nomenclature

A_{ebu}, B_{ebu}	=	model coefficient of eddy dissipation model
D	=	Rosin Rammler diameter
F	=	blending function, factor of safety in grid convergence index, thrust
f	=	parameter of grid convergence index
H	=	enthalpy, altitude
h	=	height of cruise vehicle, grid spacing
I	=	species component, specific impulse
i, j, k	=	three axes direction
k	=	turbulent kinetic energy
M	=	molecular weight, Mach number
m	=	flow rate
P	=	pressure
Pr	=	Prandtl number
p	=	order of accuracy in grid convergence index
q	=	heat flux
R_k	=	mixing rate of eddy dissipation model
S	=	source term
T	=	temperature
t	=	time
x, y, z	=	three axes direction
Y	=	species mass fraction
α	=	angle of attack
η	=	efficiency
μ	=	viscosity
ν	=	dispersion factor, stoichiometric coefficient, kinematic viscosity
ρ	=	density
τ	=	shear stress
ϕ	=	equivalence ratio
Ω	=	strain rate
ω	=	turbulent frequency

Subscripts

a	=	air
ci	=	combustor inlet
CV	=	cruise vehicle
f	=	fuel
i	=	various species
k	=	x, y, z directions
L	=	lift
o	=	oxidizer
p	=	product
rec	=	recovery
SERN	=	single expansion ramp nozzle
t	=	turbulent
0	=	total
1, 2	=	fine, coarse grid
∞	=	freestream

Received 4 December 2014; revision received 10 March 2015; accepted for publication 12 March 2015; published online 27 April 2015. Copyright © 2015 by Debasis Chakraborty, DRDL, Hyderabad 500 058. Published by the American Institute of Aeronautics and Astronautics, Inc., with permission. Copies of this paper may be made for personal or internal use, on condition that the copier pay the $10.00 per-copy fee to the Copyright Clearance Center, Inc., 222 Rosewood Drive, Danvers, MA 01923; include the code 1533-3876/ 15 and $10.00 in correspondence with the CCC.
*Directorate of Computational Dynamics, Kanchanbagh.
†Directorate of Computational Dynamics, Kanchanbagh; debasis_cfd@ drdl.drdo.in.

I. Introduction

ROCKET propulsion had dominated space launch applications for almost entirely the last half of the 20th century. These rocket system designs were refined and improved to reach their optimum limits of efficiency, performance, reliability, and safety. Hypersonic airbreathing propulsion systems have significant potential for the design and development of the transatmospheric high-speed vehicles. When the flight is in the hypersonic regime ($M_\infty > 5.0$), the burning of fuel must occur in supersonic speed inside the combustor to minimize the total pressure loss and thrust loss and allow less rise of the combustor temperature. In turn, this increases propulsive efficiency of the hypersonic systems, resulting in reduced vehicle size and weight.

A detailed review of scramjet-powered hypersonic programs, spanning over 40 years (1960–2000) in the United States, Russia, France, Germany, Japan, Australia, and other countries has been made in [1]. Although the research had started in the early 1960s, it is only in the last decade that the demonstration of scramjet-powered hypersonic flight vehicle technology in flight has been performed successfully. The successful Mach 7 flight test of the X-43A (with hydrogen fuel) research vehicle [2,3] and X-51A (with hydrocarbon fuel) [4] demonstrated the capability of airframe-integrated scramjet engine and hypersonic airbreathing vehicle design tools. Matra British Aerodynamics Aero Product France and ONERA developed a small-scale, 4.2-m-long, dual-mode, scramjet-powered experimental hypersonic vehicle [5] to demonstrate the capability of prediction of

Downloaded by DEFENSE RESEARCH & DEVLOP. LAB. (DRDL) on August 24, 2015 | http://arc.aiaa.org | DOI: 10.2514/1.B35686

aeropropulsive thrust–drag balance. A hypersonic flight experimental vehicle, Hyflex, was designed, developed, and flight tested [6] in 1996 as the precursor engineering demonstrator of the H-II Orbiting Plane program of Japan. Computational fluid dynamics (CFD) tools were used extensively for the design and analysis of various subsystems in hypersonic flight regime, like laminar/turbulent transition on forebody [7], aerothermodynamics [8], surface heating [9], scramjet combustor [10], etc. Complete vehicle analysis integrating both external and internal flow together is scarce. A posttest CFD analysis for tip-to-tail for X-43 was carried out by Voland et al. [3], however, detailed results are not available in the open literature. We could not find any studies regarding the numerical simulation of a hypersonic airbreathing vehicle with hydrocarbon fuel in the open literature.

Pannerselvam et al. [11] explained the development of hypersonic airbreathing technology in India. Demonstration of autonomous operation of a kerosene-fueled scramjet combustor at hypersonic flight speed (∼6.0–6.5) for a flight duration of about 20 s is envisaged. Although, air launch is an attractive option for a hypersonic airbreathing mission by carrying the scramjet-integrated vehicle along with the booster to certain altitudes using a high-powered aircraft, followed by acceleration to the desired Mach number by the booster and scramjet engine testing as was done in the X-43 mission. For the present configuration, a solid rocket motor booster is planned to be used to carry the scramjet-integrated cruise vehicle from ground to the desired altitude, and the scramjet-integrated vehicle would be separated and tested at the desired altitude. The scramjet combustor configuration was changed in several iterations [11–13] to meet the requirement of the hypersonic vehicle. A number of ground tests in connected pipe mode tests [12,13] and numerical simulations [14,15] were carried out to finalize the number of struts, their positions, and fuel injection locations to have a benign thermal environment and optimum performance of the flight-sized engine.

During the preliminary design phase, estimation of intake, scramjet combustor, and single expansion ram (SER) nozzle performance were carried out independently in a decoupled manner. For the high-speed airbreathing system, propulsion and aerodynamics were strongly coupled and the undersurfaces of the whole vehicle acted as a propulsion device. Hence, any demarcation of the subsystem is difficult. The coupled external–internal flow simulations would enable the designer to look at the problem in an integrated way in which thrust minus drag and other performance parameters could be obtained directly from the simulation. Hence, an integrated reacting–nonreating flow simulation for the cruise vehicle is carried out with horizontal and vertical fins, and the combustor performance and vehicle drag are evaluated. Three-dimensional Navier–Stokes equations are solved along with the shear stress transport (SST) k-ω turbulence model using the commercial CFD software CFX-11 [16]. Computations are carried out on a block structured grid generated by the ICEM-CFD [17] grid generator package. Infinitely fast rate chemistry is used for combustion modeling.

II. Geometrical Details of Cruise Vehicle with Intake, Combustor, and Single Expansion Ram Nozzle

The schematic of the hypersonic vehicle is shown in Fig. 1. The total length of the vehicle is $8.47h$ (h is the height of the vehicle). The vehicle has a rounded nose with a small radius and two ramps with 12 and 14 deg, respectively, ahead of the intake entry. The length of the intake is about $1.57h$ and that of the combustor is $2.8h$. An isolator is placed at the entry of the combustor to reduce the nonuniformity of the intake. A wall with a sweptback angle of 35 deg is placed in between the bottom and top wall of the combustor. Eight sweptback struts are arranged in symmetric manner on either side of the middle wall. Thirteen injection holes (0.4–0.5 mm diameter each) are provided on either side of the strut to inject the liquid kerosene fuel inside the combustor. The flow is exhausted into the atmosphere through a SER nozzle with a one-sided (upward) divergence angle. A bottom cowl with downward deflection is attached with the bottom wall at the exit of the combustor to provide stability and control force for the vehicle.

III. Solution Methodology

Commercial CFD software CFX-11 [16] is used for the present analysis. CFX is a fully implicit three-dimensional Reynolds-averaged Navier–Stokes (RANS) code, capable of solving diverse and complex turbulent reacting flow problems. CFX-11 implements general nonorthogonal, structured, boundary-fitted grids. The eddy dissipation model (EDM) with fast rate chemical kinetics is used for combustion of kerosene. A Rosin Rammler particle distribution [18] of diameter $D = 37.32~\mu m$ and dispersion factor of $\nu = 1.5$ is considered for droplet distribution. The Lagrangian particle tracking method is adopted to simulate the trajectory of the kerosene droplets. Turbulence was modeled using the SST k-ω turbulence model. Wall functions were used to model flow near the walls. Boundary condition details are provided next. Log-normalized maximum residue of −04 is considered as the convergence criteria.

A. Governing Equations

The system of governing equations describing the conservation of mass, momentum, energy, and species transport equations of compressible gas flows are written as follows:

Conservation of mass equation:

$$\frac{\partial \rho}{\partial t} + \frac{\partial}{\partial x_k}(\rho u_k) = 0 \qquad k = 1, 2, 3 \tag{1}$$

Conservation of momentum equation:

$$\frac{\partial}{\partial t}(\rho u_i) + \frac{\partial P}{\partial x_i} + (\rho u_i u_k) + \frac{\partial P}{\partial x_i} = \frac{\partial(\tau_{ik})}{\partial x_k}, \qquad i, k = 1, 2, 3 \tag{2}$$

Conservation of energy equation:

$$\frac{\partial}{\partial t}(\rho H) + \frac{\partial}{\partial x_k}(\rho u_k H) = -\frac{\partial}{\partial x_k}(u_j \tau_{jk}) + \frac{\partial q_k}{\partial x_k}, \qquad j, k = 1, 2, 3 \tag{3}$$

Conservation of species mass fraction Y_I:

$$\frac{\partial}{\partial t}(\rho Y_I) + \frac{\partial}{\partial x_k}(\rho u_k Y_I) = \frac{\partial}{\partial x_k}\left[\left(\frac{\mu_l}{Pr} + \frac{\mu_t}{\sigma_c}\right)\frac{\partial Y_I}{\partial x_k}\right] + S_I \tag{4}$$

where the source term S_I is due to the chemical reaction rate involving species component I, and Y_I is the mass fraction of Ith species. The chemical reactions can be described in terms of k elementary reactions involving N_C components that can be written as
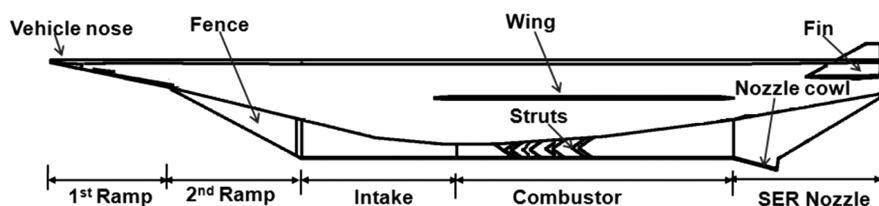

Fig. 1 Schematic of hypersonic technology demonstrator airbreathing cruise vehicle.

$$\sum_{I=A,B,C,\ldots}^{N_c} v_{kI}^i I \Leftrightarrow \sum_{I=A,B,C,\ldots}^{N_c} v_{kI}^{ii} I \qquad (5)$$

where ν_{kI} is the stoichiometric coefficient for species component I in the elementary reaction k. The rate of production/consumption S_I for species component I can be computed as the sum of the rate of progress for all the elementary reactions in which component I participates:

$$S_I = M_{wI} \sum_{k=1}^{k} (v_{kI}^{ii} - v_{kI}^i) R_k \qquad (6)$$

where M_{wI} is molecular weight of species component I, and R_k is the elementary reaction rate of progress for reaction, which can be calculated using the EDM combustion model.

1. SST k-ω Turbulence Model

To retain the robust and accurate formulation of Wilcox's k-ω model [19] in the near-wall region, and to take advantage of the freestream independence of the k-ε model [20] in the outer part of the boundary layer, Menter [21] blended both the models through a switching function. The k-ε model was transformed into Wilcox's k-ω formulation [19] and was multiplied by $(1 - F_1)$ and added to the original k-ω model multiplied by F_1. The blending function F_1 will be one in the near-wall region and zero away from the surface. In the second step, the definition of eddy viscosity μ_t was modified in the following way to account for the transport of the principal turbulent shear stress ($\tau = -\overline{\rho u' v'}$):

$$v_t = \frac{a_1 k}{\max(a_1 \omega; \Omega F_2)} \qquad (7)$$

where kinematic viscosity $\nu_t = \mu_{t/\rho}$, F_2 is a blending function similar to F_1, which restricts the limiter to the wall boundary layer, and Ω is an invariant measure of the strain rate. Their formulation is based on the distance to the nearest surface and on the flow variables:

$$F_2 = \tanh\left(\arg\frac{4}{2}\right) \qquad (8)$$
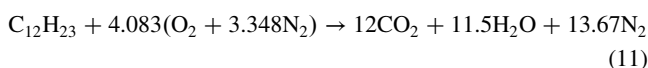
The argument is defined as

$$\arg_2 = \min\left|\max\left\{\frac{\sqrt{k}}{0.09\omega y'}, \frac{500v}{wy^2}\right\}, \frac{4\rho\sigma_{w2}k}{y^2 \mathrm{CD}_{k\omega}}\right| \qquad (9)$$

where y is the distance to the wall, and $\mathrm{CD}_{k\omega}$ is the positive portion of the cross-diffusion terms expressed as

$$\mathrm{CD}_{k\omega} = \max\left[2\rho\sigma_{\omega2}\frac{1}{\omega}\frac{\partial k}{\partial x_j}\frac{\partial \omega}{\partial x_j}, \ 10^{-20}\right] \qquad (10)$$

2. Combustion Modeling

For combustion, the eddy dissipation combustion model is used for its simplicity and robust performance in predicting reactive flows. The eddy dissipation model is based on the concept that chemical reaction is fast relative to the transport process in the flow. When reactants mix at the molecular level, they instantaneously form products. The model assumes that the reaction rate may be related directly to the time required to mix reactants at the molecular level. In turbulent flows, this mixing time is dictated by the eddy properties, and therefore the burning rate is proportional to the rate at which turbulent kinetic energy is dissipated (i.e., the reaction rate is proportional to ε/k, where k is the turbulent kinetic energy and ε is its rate of dissipation). The chemistry of the combustion reaction is represented on a molar basis by

$$\mathrm{C}_{12}\mathrm{H}_{23} + 4.083(\mathrm{O}_2 + 3.348\mathrm{N}_2) \rightarrow 12\mathrm{CO}_2 + 11.5\mathrm{H}_2\mathrm{O} + 13.67\mathrm{N}_2 \qquad (11)$$

The mixing rate, determined from the EDM, is given as

$$R_k = -A_{\mathrm{ebu}}\bar{\rho}\frac{\varepsilon}{k}\ \min\left\{Y_f, \frac{Y_o}{v_s}, B_{\mathrm{ebu}}\frac{Y_p}{1+v_s}\right\} \qquad (12)$$

where Y_f, Y_o, and Y_p are the mass fractions of fuel, oxidizer, and products respectively, $A_{\mathrm{ebu}}(= 4.0)$ and $B_{\mathrm{ebu}}(= 0.5)$ are the model constants, and v_s is the stoichiometric ratio.

B. Discretization of Governing Equations

The CFD solver uses a finite volume approach, in which the conservation equations in differential form are integrated over a control volume described around a node, to obtain an integral equation. The pressure integral terms in the momentum integral equation and the spatial derivative terms in the integral equations are evaluated using the finite element approach. An element is described with eight neighboring nodes. The advective term is evaluated using upwind differencing with physical advection correction. The set of discretized equations form a set of algebraic equations $Ax = b$, where x is the solution vector. The solver uses an iterative procedure to update an approximated x_n (solution of x at nth time level) by solving for an approximate correction x' from the equation $Ax' = R$, where $R = b - Ax_n$ is the residual at the nth time level. The equation $Ax' = R$ is solved approximately using incomplete lower-upper factorization method. An algebraic multigrid method is implemented to reduce low-frequency errors in the solution of the algebraic equations. Maximum residual $[= \varphi_j^{n+1} - f(\varphi_j^{n+1}, \varphi_j^n)] < 10^{-4}$ is taken as convergence criteria.

IV. Results and Discussion

A. Computational Domain and Grid

Considering half-symmetry along the width, only half of the vehicle geometry is considered for the simulation. To estimate the forebody–intake flowfield accurately and to avoid interaction of shocks with the far-field boundary, the computational domain is extended as follows:
1) Distance between domain inlet to vehicle nose $= h$.
2) Distance between vehicle base to domain outlet $= 2.5h$.
3) Width of the domain $= 6h$ (at inlet) and $3.5h$ (at outlet).
4) Height of domain $= 12h$ (at inlet) and $7h$ (at outlet).
The schematic of the computational domain with boundary conditions is shown in Fig. 2.

Good quality structured grids (hexahedral) are made using ICEM-CFD [17] for the complete computational domain. The total computational domain is divided into 1560 blocks, and grids were generated ensuring better orthogonality, aspect ratio, and skewness and ensuring well connectivity of the grids between the blocks. A total grid of size 22.1 million for half-geometry $[601(x) \times 224(y) \times 164(z)]$ is used in the simulations. For the grid independence study, a new grid of size 16 million $[520(x) \times 195(y) \times 158(z)]$ is generated and the reacting flow surface pressure was compared between these two grids (grid independence results are presented in Sec. IV.D.1). The grid structure
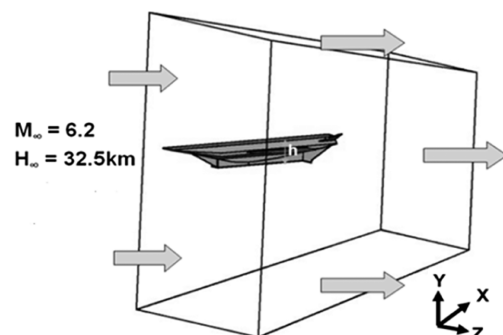

$M_\infty = 6.2$
$H_\infty = 32.5 \mathrm{km}$

Fig. 2 Computational domain.

a) Cruise vehicle   **b) Wing and fin region**   **c) Internal flow path**   **d) Scramjet combustor**
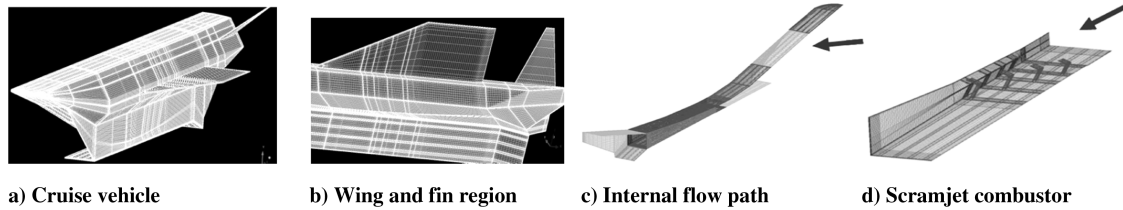
Fig. 3   Grid distribution around vehicle and internal surfaces.

on the surface of the cruise vehicle, wing and fin regions, internal flowpath, and combustor wall are shown in Fig. 3.

The grids are fine near the vehicle nose, ramps, intake entry, wings, fins, combustor strut regions, SER nozzle entry, vehicle base regions, and near-wall regions, whereas relatively coarser grids are provided in the remaining portion of the vehicle. In the simulation, the x axis is taken along the length of vehicle, whereas the y and z axes are chosen along the height and width of the vehicle, respectively, with the origin being placed at the midwidth of the combustor inlet at the bottom wall.

B.   Boundary Conditions

Simulations are carried out for freestream Mach number of 6.2 at 32.5 km altitude considering pure air (23% O_2 and 77% N_2 by mass) for 0 and 6 deg angle-of-attack conditions. Liquid kerosene fuel is injected transversely from the struts with equivalence ratio of 1.0. All the flow properties are kept constant in the inflow plane, as the inflow boundary is supersonic. No slip and adiabatic wall boundary conditions are imposed on the walls. The supersonic outflow boundary condition is applied at the exit of the computational domain. The symmetry boundary condition is imposed at the symmetry plane.

C.   Nonreacting Flow Simulation Results

Nonreacting flow simulations are performed for two angles of attack to find mass flow through the intake of the vehicle. The shocks, which are generated from the nose and forebody of the vehicle, impinge on the cowl and get reflected inside the intake, which is shown in the static pressure distribution at the x-y plane for $z/h = 0.21$ in Fig. 4. Because of the impingement of the shock on the cowl, pressure starts rising at $x/h \sim -1.75$, whereas the pressure remains constant at the body under the surface up to $x/h \sim -0.75$ and then starts rising due to the impingement of reflected shock coming from the cowl. Because of this complex shock reflection process, different axial pressure distribution (Fig. 5) is observed in the cowl and body under the surface. Shock impingement and reflection phenomena give a nonuniform pressure distribution at the intake and combustor entry, which can be observed in Fig. 6. At the combustor entry, the cowl static pressure P/P_∞ is 48 in comparison to the body under surface static pressure of 24.

The mass flow rate of air and the total pressure recovery at the entry of the intake is presented in Table 1 for two angles of attack. Mass flow rate is 26% more and pressure recovery is 34% less for angle of attack $\alpha = 6$ deg compared with $\alpha = 0$ deg.
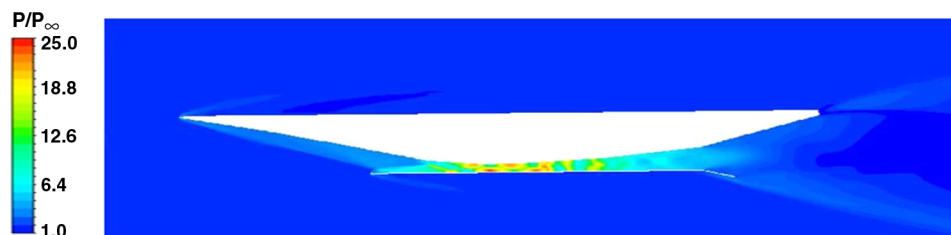
D.   Reacting Flow Simulation Results

Considering 23% of oxygen (by mass fraction) in ingested air, the kerosene fuel requirement is calculated to obtain the equivalence ratio ϕ of 1.0. The fuel is injected equally through 104 holes provided in four struts (for half-geometry). As explained earlier, two sets of reacting calculations corresponding to $\alpha = 0$ and 6 deg are considered in the present study.

1.   Angle of Attack Equal to Zero Degrees

Reacting flow simulations are carried out with transverse injection of liquid kerosene fuel into the main flow through the struts with an equivalence ratio $\phi = 1.0$. The flow features consisting of Mach number, pressure, temperature, mass fractions of carbon dioxide (CO_2), water vapor (H_2O), oxygen (O_2), and kerosene vapour ($C_{12}H_{23}$) at various axial locations of the combustor are presented to bring out the combustion characteristics in integrated mode. The wall pressures for the intake, combustor, and SER nozzle, the combustion efficiency and thrust produced by the combustor and SER nozzle are also presented.

Mach number distribution at the x-y plane (longitudinal view) at $z/h = 0.21$ (parallel to symmetry plane in between second and third strut) is shown in Fig. 6. Freestream high-speed airflow is compressed at nose, ramps, and intake of the vehicle and entered into
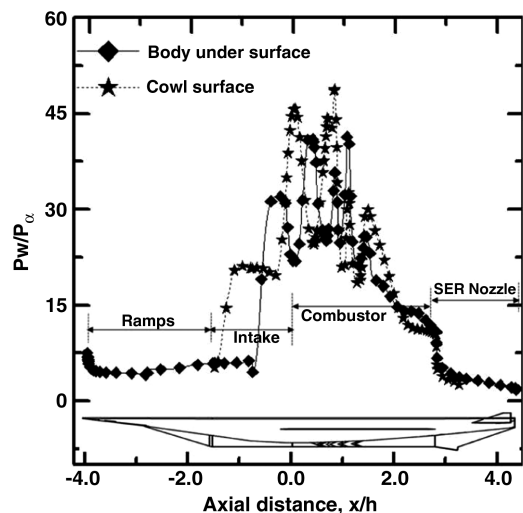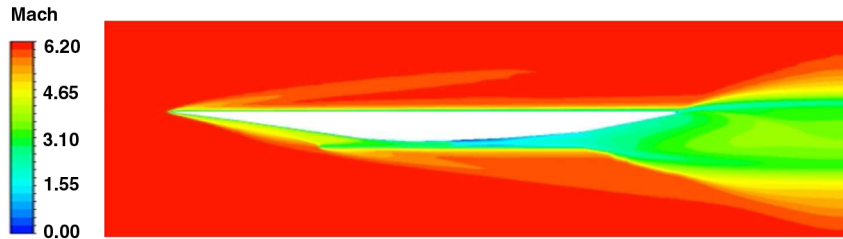

Fig. 5   Comparison of wall surface pressure.

Fig. 4   Nonreacting static pressure distribution at x-y plane ($z/h = 0.21$) for $\alpha = 0$ deg.

Fig. 6   Mach number distribution at x-y plane ($z/h = 0.21$) for $\alpha = 0$ deg.

the combustor. The flow is further decelerated inside the combustor due to the presence of the struts and combustion of kerosene fuel with the incoming air. The flow is expanded in the divergent portion of the combustor and SER nozzle. Mach number distribution is nonuniform at the combustor inlet with a high supersonic core. The nonuniformity at the combustor exit has reduced significantly.

Figure 7 presents the Mach number distribution at various cross-sectional planes [$x/h = 0$ (combustor inlet), 1.0, 2.0, and 2.8 (combustor outlet)] to depict the flow pattern in different axial stations in the combustor. The Mach number distribution at the combustor entry ($x/h = 0.0$) and the combustor outlet ($x/h = 2.8$) is nearly uniform, but a few subsonic pockets are observed in the combustion intense regions in the strut regions ($x/h = 1.0$). However, the average Mach number is found to be equal or more than unity, as seen in Fig. 8. Minimum average Mach number of about 1.18 has been observed at $x/h \sim 1.24$ from the combustor inlet. Average Mach numbers at the intake entry and combustor inlet and exit have been found to be 4.08, 2.57, and 1.82, respectively.

Area-averaged static and total pressure distribution are presented in Figs. 9 and 10, respectively. Static pressure distribution is almost the same as nonreacting flow up to the inlet of the combustor. Because of the combustion of fuel with air inside the combustor, static pressure is increased quite significantly in the intense reaction zone. However, total pressure is found to decrease continuously. Behind the struts ($x/h \sim 0.6$–0.9), the gradient for static pressure rise is maximum, whereas the reverse is true for total pressure (i.e., fall in total pressure is maximum in these regions). Average static pressure P/P_∞ at the intake entry and combustor inlet and exit has been found to be 4.67, 33.3, and 27.2, respectively. The average total pressure P/P_o at the intake entry and combustor inlet and exit have been found to be 0.466, 0.284, and 0.064, respectively, which gives a total pressure loss of 53.4, 18.2, and 22.0% of freestream total pressure from the nose to intake entry, intake entry to combustor inlet, and combustor inlet to exit, respectively.

The vehicle bottom surface wall pressure distribution corresponding to nonreacting and reacting flow have been plotted in Fig. 11 for $\alpha = 0$ deg. The train of shockwaves is clearly observed from the wall pressure distribution pertaining to nonreacting flow. The difference of pressure between the two is due to combustion of kerosene fuel with the incoming air. The surface pressure distribution for reacting flow with 16 million grids is also plotted in the figure. It is clear that, by increasing the grid point from 16 to 22.1 million, there is only marginal change in the results. An estimate of the error due to the grid in the form of the grid convergence index (GCI) is also presented in the figure. Iterative convergence or grid convergence error is the main source of numerical error in CFD for the steady-state boundary value problem. In [22,23], it was proposed an error based on the uncertainty estimate of the numerical solution named GCI as

$$\mathrm{GCI} = F_s \frac{|\varepsilon|}{(h_2/h_1)^p - 1}$$
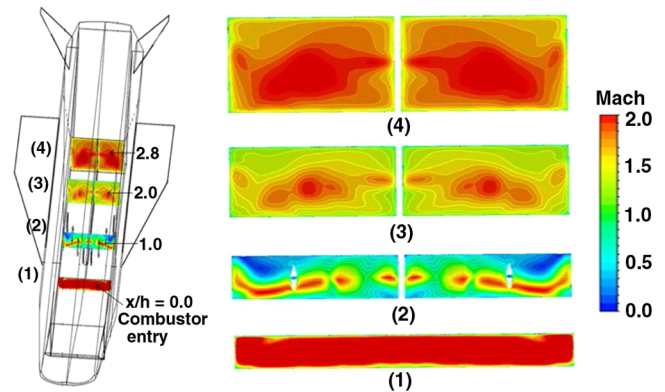

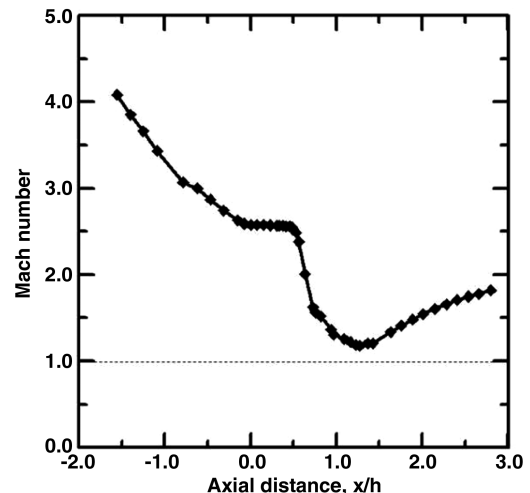Fig. 7   Mach number distribution at different axial planes.

Fig. 8   Average Mach number distribution.

where h is the order of grid spacing, p is the order of accuracy of the numerical scheme, and F_s is a factor of safety ($F_s = 3$ for minimal of two grid calculations). The relative difference between coarse and fine solution is $\varepsilon = (f_2 - f_1)/f_1$, (where f represents any quantity of interest, and the indices 1 and 2 refer to the fine and coarse grid solutions, respectively). For the present calculation, $p = 2$ with $h_2/h_1 = 2$, and GCI is on the order of ε. The same GCI-based error estimate has already been used by the authors in analyzing various reacting and nonreacting flows [14,24]. The maximum error between two simulations is within 5% with maximum deviation in the region where fuel injection struts are placed. This analysis indicates that the grid is adequate to capture most features of the flow and the solution is grid independent.

To finalize the scramjet combustor for the mission, a number of ground tests were conducted in connect pipe tests, and CFD simulations acted as a guide to the experimental studies. Various thermo-chemical parameters in the combustor obtained from CFD simulations were analyzed to select the number and location of the
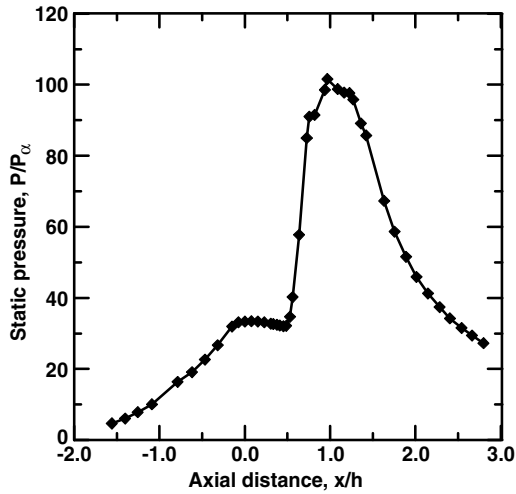
Table 1   Mass flow rate and total pressure at entry of intake

AOA, α deg	$\dot{m}_a/\dot{m}_{a_{\alpha=0}}$	$P_{\mathrm{rec}} = P_0/P_{0\infty}$
0	1.0	0.47
6	1.26	0.31

Fig. 9   Average static pressure distribution.

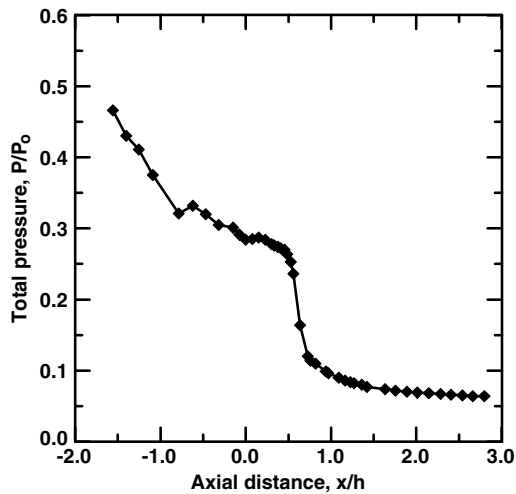Fig. 12   Comparison of test results with CFD.

Fig. 10   Average total pressure distribution.

struts and fuel injectors to get a benign thermal environment around the strut surface, while meeting the performance of the vehicle. Surface pressures measured in these ground tests were compared with computational results for both pre- and posttest conditions. Important CFD results for the flight-worthy scramjet combustor are presented in [14,25], and a typical comparison of top wall pressure
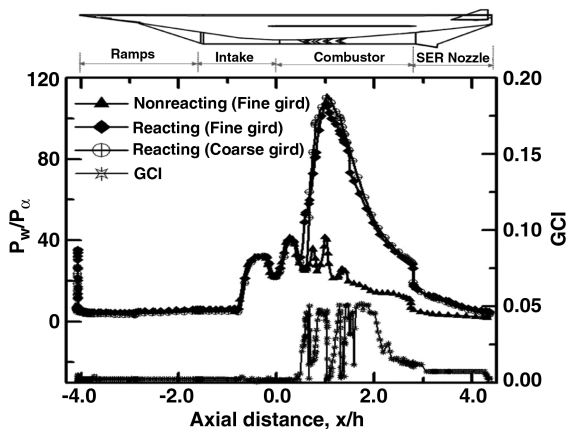
Fig. 11   Comparison of wall pressure at vehicle bottom surface and GCI along length of vehicle from nose.

distribution between the test and CFD are reproduced from [25] in Fig. 12. The occurrence of pressure rise in the computation is slightly downstream of the experimental data, and also the computation did not pick up the small pressure ups and downs upstream of the pressure rise location. No detailed exploration was done to find the cause of these differences, which may be attributed to the turbulence and combustion models employed in the simulation.

The ground test conditions were equivalent to the flight condition of $M = 6.2$, $H = 32.5$ km, and angle of attack $\alpha = 6$ deg. A very good match between experiment and CFD is obtained. Fast chemistry assumption in CFD is responsible for the higher initial peak of pressure compared with the experiment. The good comparison of reacting wall pressure forms the basis of reacting flow simulation of the complete vehicle in a reacting environment.

The distribution of static temperature at the x-y plane at $z/h = 0.21$ and the combustor inlet and exit are shown in Figs. 13a–13c, respectively. Static temperature rises at the intake and combustor inlet, due to the compression of the incoming flow at the ramps and intake of the vehicle. The temperature further rises behind the struts because of the combustion of kerosene fuel with the incoming air. Area-averaged static temperatures T/T_∞ at the intake entry and combustor inlet and exit are found to be 2.2, 4.1, and 9.4, respectively.

The axial distribution of total temperature presented in Fig. 14 shows initiation of reaction at $x/h \sim 0.6$. After $x/h \sim 1.97$, the total temperature rise is marginal, indicating the end of reaction. Nonuniformity of the temperature distribution at the combustor inlet is due to the flow compression and that at the combustor exit is due to nonuniform fuel combustion inside the combustor.

The cross-sectional distribution of CO_2 mass fractions at various axial stations [$x/h = 0$ (combustor inlet), 1.0, 2.0, and 2.8 (combustor outlet)] inside the combustor and average distribution along the length have been shown in Figs. 15a and 15b, respectively. From the figures, it is clear that the combustion of kerosene has occurred mostly in top-, mid-, and bottom-wall adjacent regions. Comparatively lesser combustion has occurred adjacent to the side-wall core regions. The mass fractions of O_2 at four locations inside the combustor and average distribution along the length have been shown in Figs. 16a and 16b, respectively. Some amount of unused O_2 has been observed toward the side-wall core regions. About 5.5% mass fraction of oxygen is still left unburnt at the exit of the combustor.

Combustion efficiency is defined as the ratio of burnt kerosene to the total amount of kerosene injected through the struts in the combustor and calculated as follows [26]:

$$\eta_{\text{combustion}} = 0.316 \frac{\int Y_{CO_2} \rho u \, dA}{\dot{m}_{C_{12}H_{23}}} \qquad (13)$$
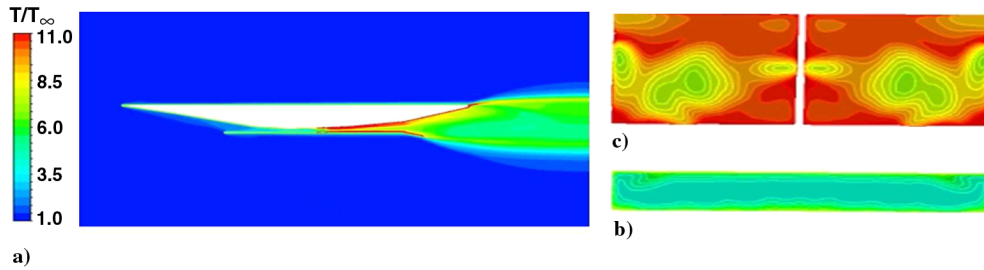
Fig. 13   Static temperature distribution at a) x-y plane, $z/h = 0.21$, b) combustor inlet, and c) combustor outlet.
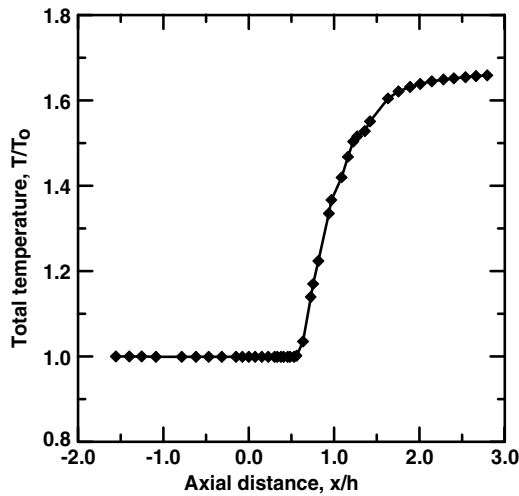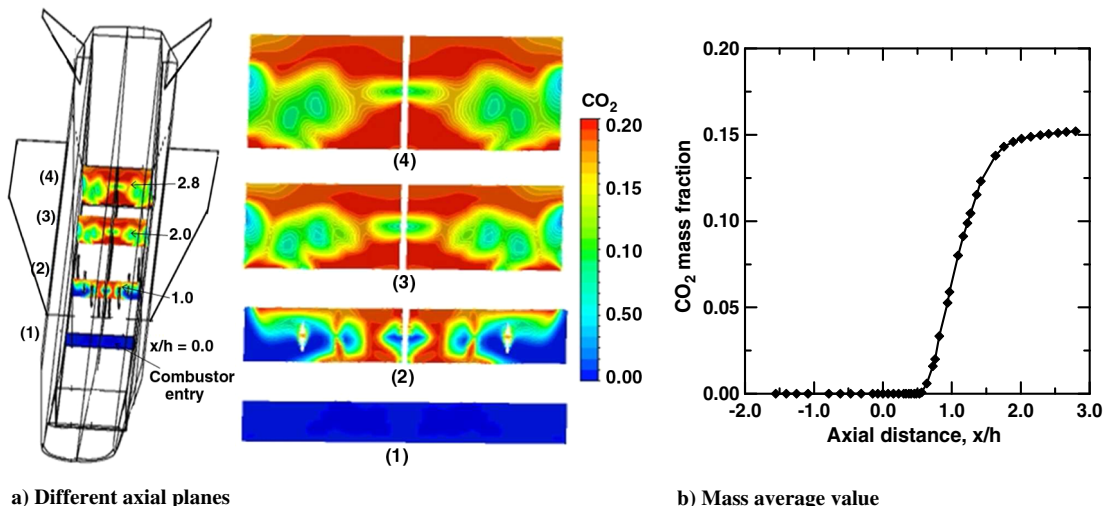

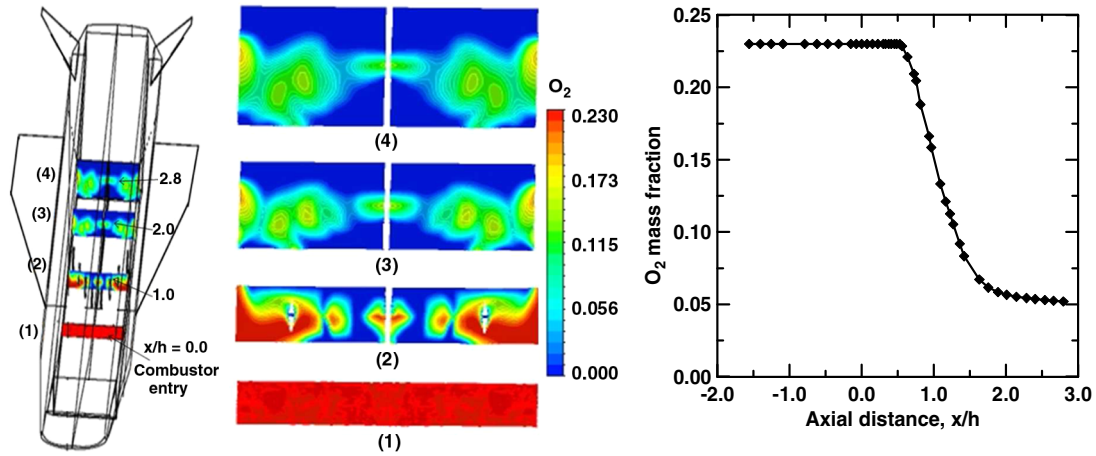**Fig. 14   Average total temperature distribution.**

2.   Results for Comparison of Six vs Zero Degree Angles of Attack

Reacting flow simulation is carried out for $\alpha = 6$ deg at $\phi = 1.0$ and results are compared with the results obtained for $\alpha = 0$ deg. Average Mach numbers in the intake and combustor are compared in Fig. 19 for two angles of attack (AOA). Though average Mach number at $\alpha = 0$ deg is more than unity everywhere along the length of the combustor (as discussed earlier), the same has become subsonic for $\alpha = 6$ deg from $x/h = 1.06$ to 1.44 with a minimum value of 0.95 obtained at $x/h = 1.22$, which is due to more kerosene burnt at $\alpha = 6$ deg.

The comparisons of the fuel flow rate, average Mach number, static and total pressure, and static and total temperature at the inlet of combustor for two angles of attack are shown in Table 2. With an increase of α, the mass flow rate of air, average static pressure, and temperature increase, whereas Mach number and total pressure decrease. The performance parameters like combustion efficiency, thrust availability from the combustor and the SER nozzle, lift, and drag are compared in Table 3. Combustion efficiency and thrust achieved increase with the increase of angle of attack. Net thrust (excluding the internal drag from struts and walls) achieved from the combustor is found to be 0.26 and 0.34 time (an increase of 30.7%) combustor inlet momentum for $\alpha = 0$ and 6 deg, respectively, whereas that from the SER nozzle alone (top surface only) is found to be 0.12 and 0.13 time (an increase of 8.3%) combustor inlet momentum, respectively.

The net positive thrust for the vehicle is found to be 0.17 and 0.21 time (an increase of 23.5%) combustor inlet momentum for $\alpha = 0$ and $\alpha = 6$ deg, respectively. The amount of lift forces produced at these two angles of attack are 0.21 and 0.74 time, respectively, showing an increase of almost 252% for the latter case. The estimated lift and drag forces are used in the vehicle stability analysis.

Pressure distributions for $\alpha = 0$ and 6 deg on the body under surface and intake-combustor bottom wall (cowl wall side) of the vehicle at $z/h = 0.21$ are compared in Figs. 20 and 21, respectively. The higher pressure level at the bottom wall compared with the top

where Y_{CO_2}, ρ, u, and $\dot{m}_{C_{12}H_{23}}$ are the mass fraction of CO_2, density of the combustion gas, axial velocity and total amount of kerosene fuel injection respectively. The cumulative combustion efficiency calculated along the length of the combustor is shown in Fig. 17.

Thrust is calculated from the difference of the local momentum F to the combustor inlet momentum F_{ci} and nondimensionalized with combustor inlet momentum F_{ci}. The negative thrust from $x/h = 0.45$ to 0.76, as shown in Fig. 18, is due to the loss of momentum caused by shocks and friction from the struts and wall surfaces. The skin friction force is calculated as $F_{sf} = \rho u_\tau A_s$, where ρ is the density, $u_\tau = 0.09^{1/4} k^{1/2}$ is the friction velocity, and k is turbulent kinetic energy. The combustion efficiency and the net thrust produced by the combustor are 76.03% and 0.26 times the combustor inlet momentum, respectively.

a) Different axial planes

b) Mass average value

Fig. 15 CO_2 mass fraction at a) different axial stations, and b) axial distribution of mass-averaged values.

a) Different axial planes   b) Mass averaged value

Fig. 16 O_2 mass fraction at a) different axial station, and b) axial distribution of mass-averaged values.
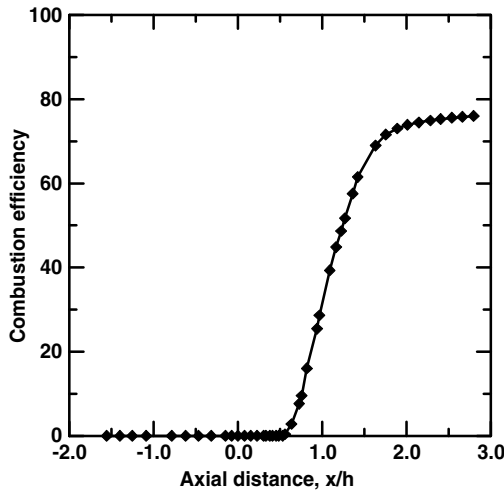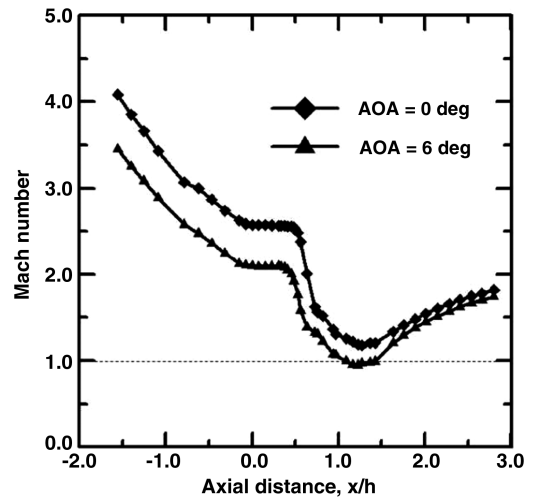

Fig. 17   Combustion efficiency along length.

Fig. 19   Comparison of area-averaged Mach number.

$\alpha = 0$ deg case. It can also be noticed from these plots that upstream influence due to combustion is contained within the combustor as the pressure rise due to combustion occurs inside the combustor.

V.   Conclusions

Nonreacting and reacting flow simulations for the complete hypersonic cruise vehicle (including forebody, intake, combustor, SER nozzle, vertical fins, and horizontal wings) are carried out considering the flow coupling of internal (reacting) and external flowfield. Three-dimensional RANS equations are solved along with the SST k-ω turbulence model, single-step chemical reaction, and Lagrangian particle tracking method using the commercial CFD
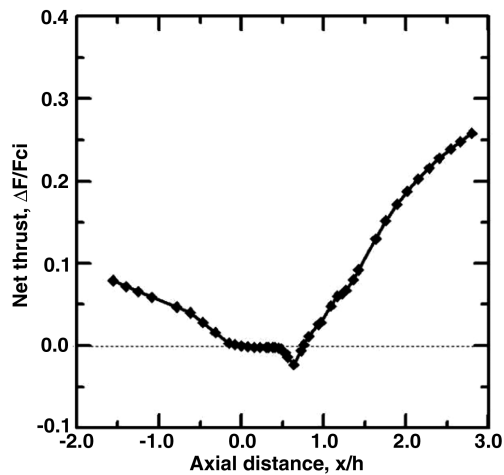

Fig. 18   Thrust profile along internal flowpath.

wall is clearly evident from these two figures. It is seen that the peak pressure level in the combustor increases by 45% for the top wall and 30% for the bottom wall compared with that at $\alpha = 0$ deg. More mass flow rate of ingested air and injected kerosene fuel for $\alpha = 6$ deg is responsible for higher pressure and thrust compared with the

Table 2   Comparison of various properties at combustor inlet

Parameters	Angle of attack	
	0 deg	6 deg
Mass flow of air, $m_a/m_{a_\alpha=0}$	1.0	1.26
Mach number, M	2.6	2.1
Static pressure, P/P_∞	33.3	57.0
Total pressure, P/P_0	0.28	0.22
Static temperature, T/T_∞	4.09	4.84
Total temperature, T/T_0	1.0	1.0

Table 3 Comparison of performance parameters for two angles of attacks

Parameters	Angle of attack	
	0 deg	6 deg
Combustion efficiency, %	76.0	81.8
Thrust (combustor), $\Delta F/F_{ci}$	0.26	0.34
Vehicle drag, D_{CV}/F_{ci}	0.21	0.26
Thrust (SER nozzle), F_{SERN}/F_{ci}	0.12	0.13
Net vehicle thrust (total thrust–drag), F_{CV}/F_{ci}	0.17	0.21
Lift force, F_L/F_{ci}	0.21	0.74
Specific impulse, I_{SP}, s	940.5	1110.7

software CFX-11. Simulations captured all the essential features of the flow, including the shocks generated from the vehicle nose and core body ramps. Various shock impingement and reflection waves in the intake and combustor top and bottom walls, which cause the nonuniformity of the flow, are crisply captured. Mass flow rate of ingested air increases with the increase of angle of attack. Average Mach number is found to be more than unity everywhere along the length of the combustor for $\alpha = 0$ deg, whereas it has become subsonic at the combustion intense zone for $\alpha = 6$ deg. Nonuniform distribution of CO_2 and O_2 mass fraction is observed at the outlet of the combustor. Some amount of unused O_2 is found toward the side-wall core regions, whereas unburnt kerosene vapors exist at the top-side wall corners at $\alpha = 0$ deg. Pressure and viscous forces for the individual struts and walls are calculated and the net thrust is determined. Higher surface pressure, and consequently higher thrust, is observed for $\alpha = 6$ deg compared with $\alpha = 0$ deg due to higher ingested air and more fuel injection for the same equivalence ratio. The net positive thrust achieved for the vehicle is found to be 0.17 and 0.21 time combustor inlet momentum for $\alpha = 0$ and 6 deg, respectively. The overall forces and moments obtained from the integrated analysis is being used in the overall mission analysis.

Acknowledgments

Fig. 20 Body under surface wall pressure along length.

Fig. 21 Intake-combustor bottom wall pressure along length.

References

[1] Curran, E. T., "Scramjet Engines: The First Forty Years," *Journal of Propulsion and Power*, Vol. 17, No. 6, 2001, pp. 1138–1148.
doi:10.2514/2.5875

[2] McClinton, C. R., Rausch, V. L., Shaw, R. J., Metha, U., and Naftel, C., "Hyper-X: Foundation for Future Hypersonic Launch Vehicles," *Acta Astronautica*, Vol. 57, No. 2, 2005, pp. 614–622.
doi:10.1016/j.actaastro.2005.03.061

[3] Voland, R. T., Huebner, L. D., and McClinton, C. R., "X-43A Hypersonic Vehicle Technology Development," *Acta Astronautica*, Vol. 59, Nos. 1–5, 2006, pp. 181–191.
doi:10.1016/j.actaastro.2006.02.021

[4] Rondeau, M. C., and Jorris, R. T., "X-51A Scramjet Demonstrator Program: Waverider Ground and Flight Test," *SFTE 44th international/ SETP Southwest Flight Test Symposium*, Soc. of Flight Test Engineers, Paper 412TW-PA-13417, Fort Worth, TX, Oct.–Nov. 2013.

[5] Fedioun, I., and Orlik, E., "Boundary Layer Transition on the LEA Hypersonic Vehicle Forebody," AIAA Paper 2012-5864, 2012.

[6] Sakurai, H., Kobayasi, M., Yamazaki, I., Shirouzu, M., and Shirouzu, M., "Development of the Hypersonic Flight Experimental Vehicle," *Acta Astronautica*, Vol. 40, Nos. 2–8, 1997, pp. 105–112.
doi:10.1016/S0094-5765(97)00149-5

[7] Lockwood, M. K., Petley, D. H., Martin, J. G., and Hunt, J. L., "Airbreathing Hypersonic Vehicle Design and Analysis Methods and Interactions," *Progress in Aerospace Sciences*, Vol. 35, No. 1, 1999, pp. 1–32.
doi:10.1016/S0376-0421(98)00008-6

[8] Gnoffo, P. A., Weilmuenster, K. J., and Hamilton, H. H., II, "Computational Aerothermo-Dynamic Design Issues for Hypersonic Vehicles," *Journal of Spacecraft and Rockets*, Vol. 36, No. 1, 1999, pp. 21–43.
doi:10.2514/2.3430

[9] Fuhrmann, H. D., Hildebrand, J., and Lalicata, T., "Aerothermodynamic Overview, X-34," *Journal of Spacecraft and Rockets*, Vol. 36, No. 2, 1999, pp. 153–159.
doi:10.2514/2.3437

[10] Manna, P., Behera, R., and Chakraborty, D., "Design and Analysis of Liquid Fueled Strut Based Scramjet Combustor—A CFD Approach," *Journal of Propulsion and Power*, Vol. 24, No. 2, 2008, pp. 274–281.
doi:10.2514/1.28333

[11] Pannerselvam, S., Thiagarajan, V., Ganesh Anavardham, T. K., Geetha, J. J., Ramanuchari, V., and Prahlada, , "Airframe Integrated Scramjet Design and Performance Analysis," International Soc. on Air Breathing Engines Paper 2005-1280, 2005.

[12] Chandrasekhar, C., Ramanujachari, V., and Kishen Kumar Reddy, T., "Evaluation of Kerosene Fuelled Scramjet Combustor Using a Combination of Cooled and Uncooled Strut," *Defense Science Journal*, Vol. 64, No. 1, Jan. 2014, pp. 5–12.
doi:10.14429/dsj.64.2733

[13] Ramanujachari, V., Chandrasekhar, C., Satya, V., and Panneerselvam, S., "Experimental Investigations of a Strut Based Scramjet Combustor Using Kerosene Fuel," *Seventh Asia-Pacific Conference on Combustion*, National Taiwan Univ., Taiwan, May 2009, Paper 10161.

[14] Manna, P., Dharavath, M., Sinha, P. K., and Chakraborty, D., "Optimization of a Flight-Worthy Scramjet Combustor Through CFD,"
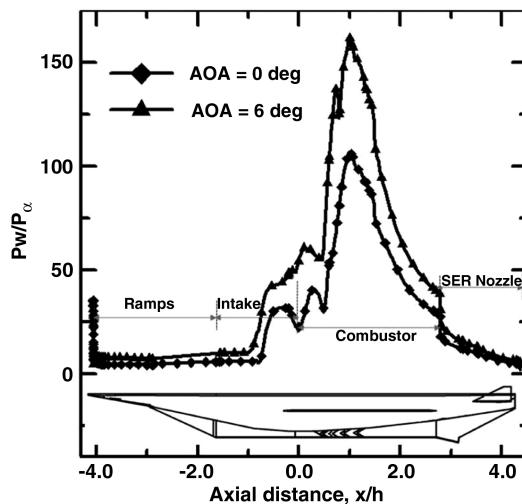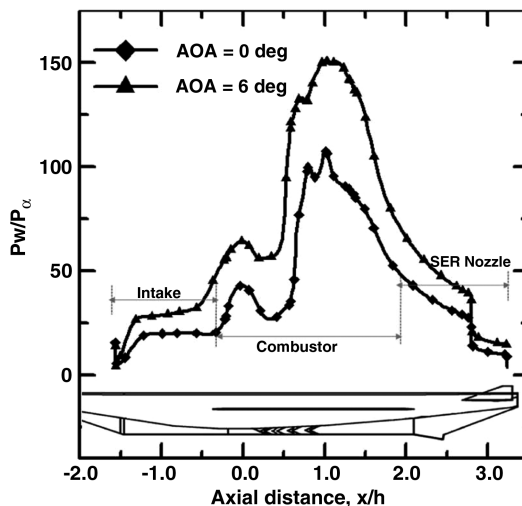
Aerospace Science and Technology, Vol. 27, No. 1, 2013, pp. 138–146.
doi:10.1016/j.ast.2012.07.005

[15] Malsur, D., Ranjith, A. R., Manoj, R., Manna, P., and Chakraborty, D., "Effect of Turbulence Models on Scramjet Combustor Performance with Kerosene Fuel," *16th AeSI CFD symposium*, CFD Division (Bangalore), Aeronautical Soc. of India Paper CP-04, Aug. 2014.

[16] ANSYS CFX, Installation and Overview, Ver. 11.0, ANSYS, Canonsburg, PA, July 2007.

[17] ANSYS ICEM-CFD-11, Installation and Overview, ANSYS, Canonsburg, PA, Jan. 2007.

[18] Kenneth, K. K., *Principles of Combustion*, Wiley-Interscience, New York, 1986, pp. 513–530.

[19] Wilcox, D. C., "Multiscale Model for Turbulent Flows," *AIAA Journal*, Vol. 26, No. 11, 1988, pp. 1311–1320.
doi:10.2514/3.10042

[20] Launder, B. E., and Spalding, D. B., "Numerical Computation of Turbulent Flows," *Computational Method in Applied Mechanical Engineering*, Vol. 3, No. 2, 1974, pp. 269–289.
doi:10.1016/0045-7825(74)90029-2

[21] Menter, F. R., "Two-Equation Eddy-Viscosity Turbulence Models for Engineering Applications," *AIAA Journal*, Vol. 32, No. 8, 1994, pp. 1598–1605.
doi:10.2514/3.12149

[22] Cutler, A. D., Danehy, P. M., O'Byrne, S., Rodrigues, C. G., and Drummond, J. P., "Supersonic Combustion Experiment for CFD Model Development and Validation," AIAA Paper 2004-266, 2004.

[23] Roache, P. J., "Error Base for CFD," AIAA Paper 2003-0408, 2003.

[24] Aswin, G., and Debasis, C., "Numerical Simulation of Transverse Side Jet Interaction with Supersonic Free Stream," *Aerospace Science and Technology*, Vol. 14, No. 5, 2010, pp. 295–301.
doi:10.1016/j.ast.2010.02.001

[25] Venugopalan, P., "Combustion Problems in Rocket Propulsion Systems," *Proceedings of Eighth Asia-Pacific Conference on Combustion*, Paper 13, The Combustion Institute—Indian Section (CIIS), Dec. 2010, pp. 52–60.

[26] Gerlinger, P., Stoll, P., Kidler, M., Schneider, F., and Aigner, M., "Numerical Investigation of Mixing and Combustion Enhancement in Supersonic Combustor by Strut Induced Streamwise Vorticity," *Aerospace Science and Technology*, Vol. 12, No. 2, 2008, pp. 159–168.
doi:10.1016/j.ast.2007.04.003

J. Oefelein
Associate Editor